The crystal structure of dGTPase reveals the molecular basis of dGTP selectivity

Christopher O. Barnes[a,b,1], Ying Wu[a,1], Jinhu Song[c], Guowu Lin[a], Elizabeth L. Baxter[c], Aaron S. Brewster[d], V. Nagarajan[e], Andrew Holmes[f], S. Michael Soltis[c], Nicholas K. Sauter[d], Jinwoo Ahn[a], Aina E. Cohen[c,2], and Guillermo Calero[a,2]

[a]Department of Structural Biology, University of Pittsburgh School of Medicine, Pittsburgh, PA 15260; [b]Department of Pharmacology and Chemical Biology, University of Pittsburgh School of Medicine, Pittsburgh, PA 15260; [c]Structural Molecular Biology, Stanford Synchroton Radiation Lightsource, SLAC National Accelerator Laboratory, Stanford University, Menlo Park, CA 94025; [d]Molecular Biophysics and Integrated Bioimaging Division, Lawrence Berkeley National Laboratory, Berkeley, CA 94720; [e]JAN Scientific Inc., Seattle, WA 98105; and [f]Swanson School of Engineering, University of Pittsburgh, Pittsburgh, PA 15260

Edited by Alexander M. Klibanov, Massachusetts Institute of Technology, Cambridge, MA, and approved March 22, 2019 (received for review November 26, 2018)

Deoxynucleotide triphosphohydrolases (dNTPases) play a critical role in cellular survival and DNA replication through the proper maintenance of cellular dNTP pools. While the vast majority of these enzymes display broad activity toward canonical dNTPs, such as the dNTPase SAMHD1 that blocks reverse transcription of retroviruses in macrophages by maintaining dNTP pools at low levels, *Escherichia coli* (*Ec*)-dGTPase is the only known enzyme that specifically hydrolyzes dGTP. However, the mechanism behind dGTP selectivity is unclear. Here we present the free-, ligand (dGTP)- and inhibitor (GTP)-bound structures of hexameric *Ec*-dGTPase, including an X-ray free-electron laser structure of the free *Ec*-dGTPase enzyme to 3.2 Å. To obtain this structure, we developed a method that applied UV-fluorescence microscopy, video analysis, and highly automated goniometer-based instrumentation to map and rapidly position individual crystals randomly located on fixed target holders, resulting in the highest indexing rates observed for a serial femtosecond crystallography experiment. Our structures show a highly dynamic active site where conformational changes are coupled to substrate (dGTP), but not inhibitor binding, since GTP locks dGTPase in its apo- form. Moreover, despite no sequence homology, *Ec*-dGTPase and SAMHD1 share similar active-site and HD motif architectures; however, *Ec*-dGTPase residues at the end of the substrate-binding pocket mimic Watson–Crick interactions providing guanine base specificity, while a 7-Å cleft separates SAMHD1 residues from dNTP bases, abolishing nucleotide-type discrimination. Furthermore, the structures shed light on the mechanism by which long distance binding (25 Å) of single-stranded DNA in an allosteric site primes the active site by conformationally "opening" a tyrosine gate allowing enhanced substrate binding.

serial femtosecond crystallography | X-ray free-electron laser | metalloenzymes | dNTP triphosphohydrolase

Cellular regulation of deoxynucleotide triphosphate (dNTP) pools is a vital process for DNA replication and survival in both prokaryotic and eukaryotic cells. It is tightly controlled by deoxynucleotide triphosphohydrolases (dNTPases) through hydrolyzing dNTPs into deoxynucleosides and inorganic triphosphate, in contrast to ribonucleotide reductase, which supplies cellular dNTP pools by converting ribonucleotides to the corresponding deoxy forms (1–6). As a class of metalloenzymes, dNTPases contain a histidine–aspartate (HD) motif, which helps coordinate a divalent cation near the active site to promote phosphohydrolase activity (2, 7–12). Given the importance of intracellular dNTP concentrations for cellular survival, studies have shown that tight control of dNTP pools by dNTPases can function as a host mechanism in the cellular defense against pathogens. For example, in primates the sterile alpha motif (SAM) and HD domain-containing protein 1 (SAMHD1) (13) block reverse transcription of retroviruses (e.g., HIV-1, SIV) by maintaining dNTP pools at low levels in infected cells (7–10, 12, 14). In addition, observations in prokaryotes have revealed a dNTPase–pathogen interplay, illustrated by *Escherichia coli* (*Ec*) dGTPase, where the gene 1.2 product encoded by bacteriophage T7 inhibits *Ec*-dGTPase to promote productive infection (15).

Crystal structures of the broadly acting tetrameric dNTPases, exemplified by SAMHD1, have enabled a better understanding of phosphohydrolase activity by revealing the binding modes of activator or allosteric regulator nucleotides, as well as dNTP substrates (10–12, 16). However, unlike the vast majority of dNTPases displaying broad activity toward canonical and noncanonical dNTPs (11, 12, 14, 17, 18), *Ec*-dGTPase displays a strong preference for hydrolyzing only dGTP substrates (2, 10, 11, 14, 16, 18, 19). The structural basis of *Ec*-dGTPase specificity toward dGTP is less well understood despite recent crystal structures of a free and ssDNA-bound *Ec*-dGTPase (20). Indeed, the potential of ssDNA cofactors affecting the dGTP-binding site (20, 21) suggests a unique mechanism significantly different in the allosteric activation of phosphohydrolase activity compared with other dNTPase enzymes.

Significance

While cellular dNTPases display broad activity toward dNTPs (e.g., SAMHD1), *Escherichia coli* (*Ec*)-dGTPase is the only known enzyme that specifically hydrolyzes dGTP. Here, we present methods for highly efficient, fixed-target X-ray free-electron laser data collection, which is broadly applicable to multiple crystal systems including RNA polymerase II complexes, and the free *Ec*-dGTPase enzyme. Structures of free and bound *Ec*-dGTPase shed light on the mechanisms of dGTP selectivity, highlighted by a dynamic active site where conformational changes are coupled to dGTP binding. Moreover, despite no sequence homology between *Ec*-dGTPase and SAMHD1, both enzymes share similar active-site architectures; however, dGTPase residues at the end of the substrate-binding pocket provide dGTP specificity, while a 7-Å cleft separates SAMHD1 residues from dNTP.

Author contributions: C.O.B., Y.W., J.A., A.E.C., and G.C. designed research; C.O.B., Y.W., J.S., G.L., E.L.B., A.S.B., V.N., and A.H. performed research; C.O.B., A.H., and G.C. were responsible for MCH design; C.O.B., J.S., G.L., V.N., S.M.S., and A.E.C. were responsible for imaging and incorporation of data collection software at LCLS-XPP beamline; C.O.B., Y.W., E.L.B., A.S.B., N.K.S., and G.C. analyzed XFEL data; C.O.B., Y.W., and G.C. refined and analyzed all structures; and C.O.B., Y.W., J.A., A.E.C., and G.C. wrote the paper.

The authors declare no conflict of interest.

This article is a PNAS Direct Submission.

Data deposition: Structures reported in this paper have been deposited in the Protein Data Bank, www.rcsb.org/pdb/ (accession nos. 6OI7 and 6OIV–6OIY).

[1]C.O.B. and Y.W. contributed equally to this work.

[2]To whom correspondence may be addressed. Email: acohen@slac.stanford.edu or guc9@pitt.edu.

This article contains supporting information online at www.pnas.org/lookup/suppl/doi:10.1073/pnas.1814999116/-/DCSupplemental.

Published online April 24, 2019.

In the present work, we aimed to understand the structural basis of *Ec*-dGTPase substrate specificity and the mechanism of phosphohydrolase activity in the presence of nucleotide substrates. Given that Mn^{2+} is required for optimal dGTPase activity, which can be functionally replaced by Mg^{2+} (2, 18, 22), we determined the radiation-damage free crystal structure in the presence of Mn^{2+} cations to 3.2 Å using data collected at the Linac Coherent Light Source (LCLS) X-ray Free Electron Laser (XFEL). These experiments employed a methodology for highly efficient serial femtosecond crystallography (SFX) experiments using micrometer-sized crystals that builds upon conventional crystal visualization and fixed target diffraction techniques (23, 24). Our methodology combines (*i*) the use of specialized multicrystal holders (MCH) compatible with cryo-protectant or native crystallization conditions, (*ii*) the identification of individual microcrystals on MCHs through the analysis of UV-microscopy images, and (*iii*) the development of automated routines for serial positioning of the identified crystals during data collection. Implementation of these methods improved on similar reference and alignment schemes (25–31) enabling rapid mapping and positioning of multiple crystals in random locations on the holder, which consistently resulted in >80% crystal hit-rates and the highest indexing rates reported to date for any SFX experiment.

In addition, we investigated substrate specificity by applying chemical cross-linking methods to introduce nucleotide substrates into the catalytic site of *Ec*-dGTPase crystals and obtained dGTP-, dGTP-1-thiol–, and GTP-bound *Ec*-dGTPase structures. We found that structural elements from an adjacent monomer, which protrude into the enzymatic active site, are responsible for nucleotide discrimination and dGTP specificity. Analysis of catalytic residues and Mn^{2+} cations of free and bound *Ec*-dGTPase structures revealed a regulatory mechanism for Tyr^{272} that may explain activation or inhibition by ssDNA and GTP, respectively. Overall, these structures provide detailed mechanistic insights into *Ec*-dGTPase function and demonstrate a conserved binding mode for nucleotide substrates across dNTPase enzymes.

Results

XFEL Data Collection of Microcrystals on MCHs. To address the scarcity of XFEL beam time, we sought to improve the efficiency and reliability of data collection methods by simplifying related sample preparation and operational requirements for fixed-target setups. To this end, we developed an MCH (*SI Appendix*, Fig. S1 *A* and *B*) capable of holding microcrystals under native- or cryo- crystallization conditions that is compatible with UV fluorescence microscopy for crystal imaging and identification (Fig. 1; *SI Appendix*, Fig. S1; *Methods*). Given the high contrast of the UV-fluorescence signal of crystals versus the solvent background, bright areas corresponding to the location of individual crystals on MCHs were identified and mapped relative to four fiducial marks (Fig. 1*B* and *SI Appendix*, Fig. S1). Algorithms previously incorporated into the Blu-Ice/DCSS experimental control system to position grid-based sample holders and microfluidic traps at LCLS-XPP (23, 26, 27) were adapted to automatically position crystals based on their relationship to the four fiducial coordinates of the MCH for efficient serial diffraction experiments (Fig. 1*B* and *SI Appendix*, Fig. S1 *D* and *E* and Table S1). To demonstrate this technology, our protocol was applied to various crystal morphologies generated from either *Ec*-dGTPase or RNA polymerase II (Pol II) complexes mounted on MCHs (*SI Appendix*, Fig. S1) collected during the same 24-h XFEL shift. Our methods enabled diffraction data to be collected in an automated fashion with improved intensities for high-angle Bragg reflections, consistent with previous results using MCHs (32, 33).

In addition, we implemented multishot data collection strategies for crystals measuring >100 μm along a single axis (*SI Appendix*, Fig. S1 *F–I*). Similar to helical data collection protocols at LCLS, translation of ~50 μm into uncompromised crystal volumes with angular offsets from the origin was introduced to increase dataset completeness and limit the effects of radiation or mechanical damage introduced from previous exposures (23, 24, 34). To test if microcrystals displayed problems of preferential orientation on the MCH surface, we analyzed the reciprocal basis vectors for indexed *Ec*-dGTPase and Pol II crystals that were singly exposed for one MCH (*SI Appendix*, Fig. S2) and for the entire *Ec*-dGTPase dataset (Fig. 1*C*), using described methods (35). Our results revealed a spherical-like projection indicative of randomly oriented crystals on MCHs (23, 24, 26, 34). As a result, all datasets collected showed >90% completeness to high resolution (*SI Appendix*, Table S2), with only 221 still images being required to solve the structure of the free *Ec*-dGTPase enzyme and <1,000 images for Pol II complexes (further analysis of Pol II structures is beyond the scope of this work). Overall, application of MCH methodologies resulted in efficient data collection with minimal background scattering to preserve weak Bragg reflections, highly accurate microcrystal hit rates (>80%), increased indexing rates, and dataset completeness from a minimal number of exposed crystals (*SI Appendix*, Table S2).

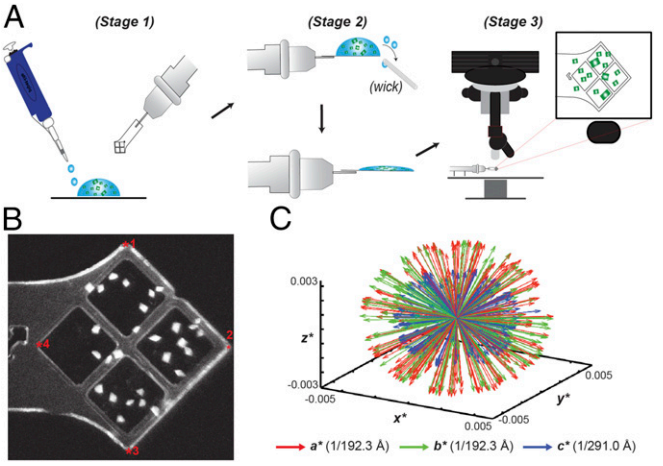

Fig. 1. Loading and mapping of crystals on MCHs. (*A*) Schematic representation of MCH loading as detailed in *Methods*. (*B*) UV-microscopy image of Pol-Spt4/5 mounted crystals. Fiducial marks are indicated by a red asterisk. (*C*) Reciprocal space representation of the basis vectors of 221 indexed dGTPase images demonstrating the lack of preferential alignment when mounting in MCHs.

Comparison of Synchrotron and XFEL Ec-dGTPase Structures. To gain structural insight into the effects of radiation-induced damage at the metal-binding site, we compared *Ec*-dGTPase structures determined from an individual crystal collected at a synchrotron source with our XFEL dataset. The synchrotron-based structure was solved from selenium–methionine derivatized protein to 2.9 Å resolution (Fig. 2*A* and *SI Appendix*, Fig. S2*A* and Table S3) and is consistent with previously published dGTPase apo-structures from *Pseudomona syringae* [Protein Data Bank (PDB) ID code 2PGS], *E. coli* (PDB ID code 4XDS), and the *E. coli* structure bound to ssDNA, PDB ID code 4X9E). Interestingly, inspection of the anomalous map revealed the presence of density within HD-motif residues His^{69}, His^{117}, and Asp^{268} (*SI Appendix*, Fig. S2*B*). Given that the crystallization condition did not contain any anomalous scatters, it was inferred that the observed signal was due to a metal bound to the protein during cell growth. A fluorescence scan of the crystals showed a peak at the Mn^{2+} edge (6.53 keV) but not at the Fe^{2+} edge (7.1 keV), suggesting the presence of Mn^{2+} ions in our crystals. This is consistent with kinetic experiments that showed Mn^{2+} (at 20 μM) as the preferred cofactor, despite similar kinetic activity achieved with 12 mM $MgCl_2$ (8).

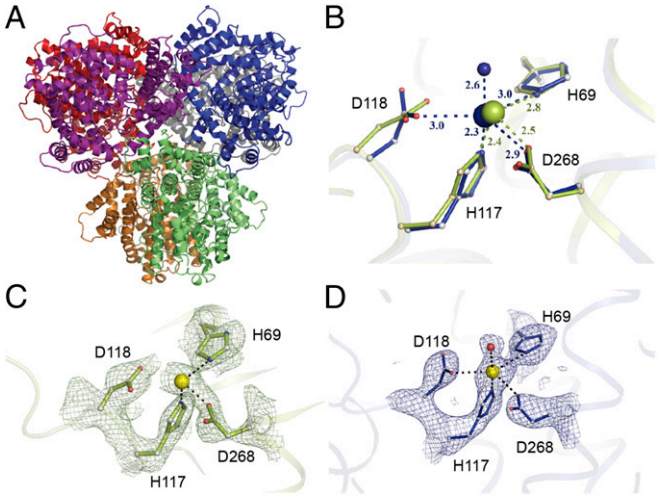

Fig. 2. The hexameric *Ec*-dGTPase XFEL crystal structure. (*A*) Cartoon representation of the hexameric *Ec*-dGTPase XFEL crystal structure solved using 221 still images from randomly oriented crystals. (*B*) Differences in Mn^{2+} coordination for XFEL (blue) and low-dose synchrotron structure (olive green). Potential H-bond interactions with distances shorter than 3.5 Å are indicated as dashes between residues. (*C*) Electron density of the Sigma-A weighted $2F_{obs} - F_{calc}$ map contoured at 1.5σ for residues comprising the HD motif (synchrotron data); Mn^{2+} ion is illustrated as a yellow sphere. (*D*) Electron density of the Sigma-A weighted $2F_{obs} - F_{calc}$ map contoured at 1.5σ for residues comprising the HD motif (XFEL data). A water molecule (indicated in red) forms part of the Mn^{2+} coordination (*SI Appendix*, Fig. S2*C*).

The radiation damage-free XFEL structure of the *Ec*-dGTPase apo-enzyme to 3.2 Å was solved from <150 crystals exposed to the XFEL beam (Fig. 2), representing the fewest number of randomly oriented microcrystals used to obtain a complete SFX dataset. Initial phases were generated by molecular replacement using the selenium–methionine phased structure. The initial unbiased sigma A-weighted difference map ($F_0 - F_{calc}$) of the radiation damage-free XFEL structure showed electron density for the Mn^{2+} ion coordinated by the HD motif residues (His^{69}, His^{117}, Asp^{118}, and Asp^{268}) (Fig. 2*B* and *SI Appendix*, Fig. S2*C*). Overlay of the HD motif residues from the synchrotron and XFEL-derived structures showed that Asp^{118} in the XFEL structure was on average 0.5–0.7 Å closer to the Mn^{2+} ion (across all six monomers) compared with the Se-Met apo-structure, which had an averaged absorbed X-ray dose of 3.4 MGy (Fig. 2 *C* and *D*). This positional difference places Asp^{118} in the XFEL structure within the coordination sphere of the catalytic metal and suggests that at even fairly low X-ray doses, radiation damage is accrued site-specifically around metal centers, possibly through the decarboxylation of the neighboring aspartic acid residue (36).

Structural Basis for dGTP Binding and Phosphohydrolase Activity. Next, we wanted to characterize the substrate-bound form of *Ec*-dGTPase by determining the structure in the presence of dGTP and the nonhydrolyzable dGTP analog, dGTP-1-thiol. Initial cocrystallization experiments of *Ec*-dGTPase with Mn^{2+} ions and dGTP-1-thiol revealed no ligand-bound structures, likely due to the high-salt condition (1.8 M ammonium sulfate) from which the crystals were harvested. Thus, we employed chemical cross-linking using glutaraldehyde to stabilize the integrity of the crystal lattice, while decreasing the salt concentrations to physiological levels for overnight soaking experiments with dGTP or dGTP-1-thiol (*Methods*). Crystals remained stable during this procedure resulting in conventional synchrotron-based structures with bound substrates and metals in all active sites (*SI Appendix*, Fig. S3 *A–E*). Cross-linked *Ec*-dGTPase crystals also showed catalytic activity when incubated with dGTP, suggesting that the cross-linked enzyme was capable of binding and hydrolyzing the dGTP substrate, albeit in a slightly diminished capacity compared with unmodified enzyme (*SI Appendix*, Fig. S3*B*).

Comparisons between the substrate-bound and apo-structures show a root mean square deviation (rmsd) of 0.9 Å for the catalytic versus 0.3 Å for the noncatalytic regions of the protein. These differences are a result of conformational changes induced by dGTP binding, as active-site residues rearrange to provide a tight-fitting pocket for the substrate (Fig. 3 *A* and *B*). Critical residues involved in dGTP binding, as well as dGTP-1-thiol binding, include (*i*) π-π stacking interactions between the electron-rich aromatic ring of Phe^{391} and the guanosine ring; (*ii*) hydrogen bonding between Arg^{433}, Arg^{442}, Glu^{400}, and Val^{54} and the guanosine ring; (*iii*) stacking interactions between Tyr^{272} [a highly conserved tyrosine found within dNTP triphosphohydrolases (14, 18, 37)] and the deoxyribose ring; (*iv*) 3′-OH discrimination via Gln^{53} and Asp^{276}; (*v*) interactions of the α-phosphate with Mn^{2+}; and (*vi*) interactions with the β- and γ-phosphates through Asn^{186}, Lys^{211}, Tyr^{212}, and Lys^{232} (Fig. 3 *C* and *D* and *SI Appendix*, Fig. S3 *C–E*). The full octahedral coordination of the Mn^{2+} ion was also visualized in the substrate-bound structure, comprising the four residues of the HD motif, a water molecule (W_1), and an oxygen molecule from the dGTP α-phosphate that replaces the coordinated water observed in the apo- XFEL structure (Fig. 3*D*). Moreover, among the six hexamers, His^{126} was found as two conformers, the first one occupying a similar position as the substrate-free structure and the second one positioned in-line with the hydroxyl group of the dGTP α-phosphate (Fig. 3*A*). This latter conformation is consistent with the proposed nucleophilic substitution reaction mechanism for dNTP hydrolysis via a nearby water molecule (35).

Owing to the contrast in side-chain confirmation for free- and substrate-bound structures, as well as the observed "sandwiching" between Tyr^{272}, His^{126}, and the dGTP ligand (Fig. 3*C*), we mutated

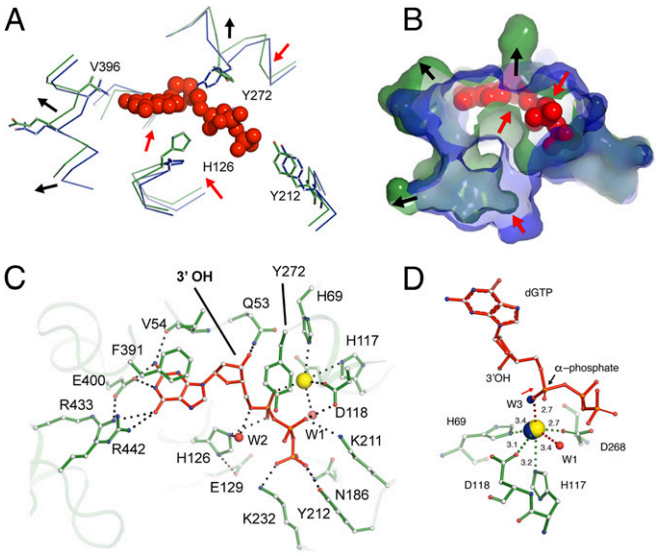

Fig. 3. Interactions of dGTP substrate with *Ec*-dGTPase. Wire (*A*) and surface (*B*) representations of the overlay between the apo- (blue) and dGTP-bound (green) structures showing the conformational changes observed in the active-site pocket upon dGTP binding (red spheres). Red arrows indicate contraction, and black arrows indicate expansion of the pocket. (*C*) Ball-and-stick representation of key residues (green) involved in dGTP (red) binding. Hydrogen bonds are illustrated as dashes and water molecules as red spheres. (*D*) Ball-and-stick representation of Mn^{2+} (yellow sphere) coordination by dGTP residues (green). Distances are indicated next to dashes. The position of the apo-XFEL Mn^{2+} ion and coordinating water after overlay with the dGTP bound-structure are indicated as blue spheres.

these residues to alanine to identify their roles in phosphohydrolase activity. The single alanine mutation in the active site had no effect on expression, purification, or hexamer formation for the H126A, E129A, or Y272A variants compared with wild type. Thus, we assayed enzymatic activity by monitoring deoxyguanosine product formation using reverse-phase chromatography. All three variants had abolished hydrolytic activity compared with wild-type enzyme, even after a 2-h incubation in the presence of 100 μM dGTP and 5 mM $MgCl_2$ (*SI Appendix*, Fig. S3*G*). While the roles of His^{126} and Glu^{129} in catalysis have been well-established (10, 37), the function of Tyr272 is less clear. Similar to structures of the tetrameric dNTPases [PDB ID code 3IRH, PDB ID code 4TNQ, PDB ID code 2DQB (9, 11, 37)], His^{126} and Glu^{129} form a catalytic dyad, by which Glu^{129} plays a role in positioning His^{126} in-line with the α-phosphate during catalysis. Interestingly, while mutations in the catalytic dyad showed slight product formation at the 2-h time point, the Y272A variant resulted in a consistently inactive enzyme (*SI Appendix*, Fig. S3*G*). This suggests that Tyr^{272} plays a critical role in *Ec*-dGTPase phosphohydrolase activity, possibly by stabilizing the α-phosphate for nucleophilic attack.

Characterization of Ec-dGTPase Specificity and Nucleotide Discrimination. Since *Ec*-dGTPase shows a very high affinity and preference for dGTP substrates (2, 18), we determined the mode by which the enzyme can specifically recognize this substrate compared with other purine or pyrimidine rings, namely dTTP, dATP, and dCTP. Recognition of dGTP within the active site is achieved by Glu^{400} and the backbone carbonyl of Val^{54}, which interacts with the purine amine groups. In addition, residues Arg^{433} and Arg^{442} project into the binding pocket from an adjacent monomer to interact with the ketone group of the purine ring (Fig. 3*C* and *SI Appendix*, Fig. S3*E*). These residues create a tight fit around the substrate by forming an extensive hydrogen bond network of interactions that stabilize dGTP for subsequent hydrolysis (Fig. 3 *B* and *C*). In contrast, modeling of dTTP, dATP, and dCTP binding to the active site shows that these nucleotides bind loosely in the pocket (due to their smaller size) and establish fewer hydrogen bonds with the purine or pyrimidine rings (*SI Appendix*, Fig. S3*H*).

GTP Binding and Inhibition of Ec-dGTPase Activity. Given that *Ec*-dGTPase showed high specificity toward the guanosine ring, and cellular nucleotide concentrations of GTP can achieve levels 100- to 1,000-fold higher than dGTP (36, 37), we suspected that GTP may play a role in *Ec*-dGTPase cellular regulation. To test our hypothesis, we analyzed the effects of GTP on *Ec*-dGTPase activity in the presence of 100 μM dGTP. We observed a negative correlation between increasing GTP concentration and decreased *Ec*-dGTPase activity (Fig. 4*A*), suggesting that at physiologically relevant nucleotide ratios (>10:1 GTP:dGTP concentrations) GTP can act as a competitive inhibitor of *Ec*-dGTPase, resulting in the loss of dGTP hydrolysis (Fig. 4*A*). To further understand this result, we obtained the structure of the GTP-bound enzyme to 3.25 Å by similar cross-linking and soaking methods under physiological conditions.

Analogous to the dGTP and dGTP-1-thiol structures, GTP was observed in all six active sites. Superposition of the dGTP- and GTP-bound structures revealed conformational changes to the overall architecture of the active-site pocket (rmsd of 1.2 Å for 155 Cα atoms that comprise the active site), as well as differences relative to substrate binding (Fig. 4 *B* and *C* and *SI Appendix*, Fig. S4*A*). In contrast to the dGTP-bound structure, the ribose 2′-OH of GTP occupies the position of the 3′-OH (in the dGTP-bound form), and the ribose 3′-OH draws closer to the Mn^{2+} ion, becoming part of its coordination sphere (Fig. 4*B*). As a result, GTP does not bind deeply in the pocket, losing interactions with the carbonyl of Val^{54}, which allows Tyr^{27} to stack against the purine ring and reach within hydrogen bond distance of the

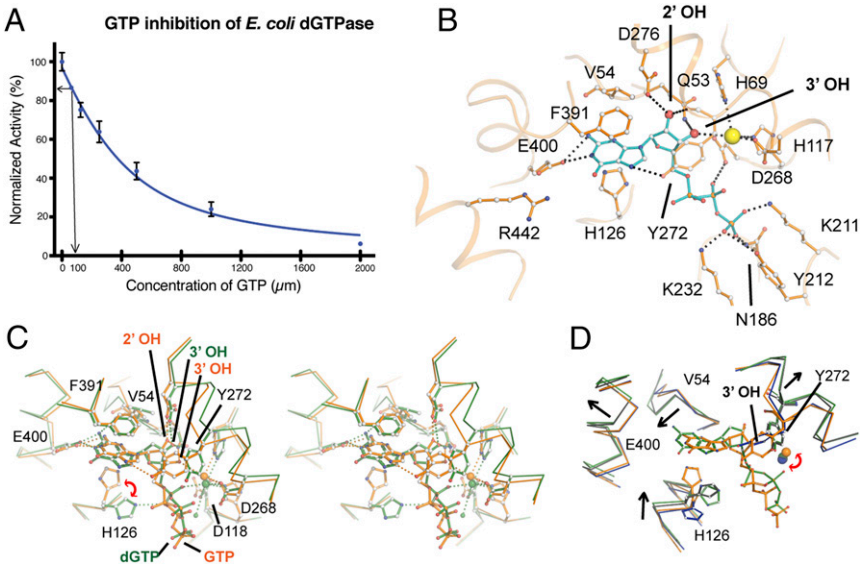

Fig. 4. Inhibition of *Ec*-dGTPase activity by GTP. (*A*) Activity of *Ec*-dGTPase in the presence of increasing concentrations of GTP (μM) and 100 μM dGTP substrate. Enzymatic activity assays were repeated three times, and the SD was plotted ($n = 3$). The arrows indicate dGTPase activity in the presence of 100 μM GTP. (*B*) Ball-and-stick representation and potential hydrogen bond interactions (black dashes) between GTP (cyan) and active-site residues of dGTPase (orange). Asp^{276} and Gln^{53} form H-bonds with the 2′-OH and the 3′-OH, respectively. Coordination of the metal by an oxygen from the α-phosphate in the dGTP-bound form is swapped by the 3′-OH of the ribose, resulting in 1.5 Å displacement with respect to its position in the dGTP-bound form; as result of this positional change, HD motif residue Asp^{118} no longer forms part of its coordination sphere. (*C*) Stereo and ball-and-stick representations of the overlay between the dGTP- (green) and the GTP-bound (orange) structures illustrating that the two binding pockets differ significantly. (*D*) Overlay of the substrate-bound structures (dGTP and dGTP-1-thiol, green and black, respectively) with the XFEL-apo and GTP-bound (inhibited) structures (blue and orange) illustrating that GTP binding "locks" the active site hindering the conformational changes observed during substrate binding. The rmsd differences between active-site residues for XFEL, dGTP, dGTP-1-thiol, and GTP are summarized in *SI Appendix*, Table S3.

α-phosphate, pulling it away from the coordination sphere of the Mn^{2+} ion (Fig. 4 *B* and *C*). Intriguingly, overlay of the active sites for the GTP-bound and apo- *Ec*-dGTPase structures shows minimal conformational changes between the two states (rmsd of 0.39 Å on 155 Cα atoms comprising the active site; Fig. 4*D* and *SI Appendix*, Fig. S4 *B* and *C*). Thus, in contrast to the extensive conformational changes observed during dGTP binding (*SI Appendix*, Fig. S4*B*), GTP does not induce a transitional "catalytic state" of the active site.

Discussion

Despite recent *Ec*-dGTPase structures detailing the potential of ssDNA acting as an effector molecule, fundamental questions about dGTP recognition and dGTPase activity regulation have not been elucidated. The work presented herein establishes (*i*) unique approaches in both XFEL and cross-linking methodologies useful to the general crystallographic community for structure determination and (*ii*) a comprehensive structural framework for understanding dGTPase substrate recognition and activity.

We detailed protocols for fixed-target data collection at XFEL sources in an automated fashion (Fig. 1 and *SI Appendix*, Figs. S1 and S2). Notwithstanding the proven success of the injector setups for structure determination, goniometer-based fixed-target approaches at the XFEL are advantageous for (*i*) data collection using delicate crystals, (*ii*) crystals in limited supply, (*iii*) large, radiation-sensitive crystals, or (*iv*) crystal quality screening to prepare for injector-based experiments. Our highly efficient fixed-target data collection methodology was demonstrated to provide greater than 80% crystal hit rates for SFX experiments using randomly oriented micrometer-sized crystals with varying morphologies. While crystals in MCHs were mapped before the experiment using UV-fluorescence microscopy at the home laboratory, improvements to the standard goniometer setup in the LCLS MFX instrument (38) will incorporate UV-imaging capabilities for "on-the-fly" crystal identification and mapping. This will improve the precision of crystal positioning and provide a straightforward means to fully automate fixed-target SFX experiments using a variety of MCH form factors. As UV imaging is broadly applicable to identify a wide range of macromolecular crystals, the general crystallographic community may easily adopt this fully automated approach for multicrystal experiments at both synchrotron and XFEL sources. This method is also compatible with new methods for in situ crystal growth and data collection (Martiel, Müller-Werkmeister and Cohen, see ref. 39).

The success of our approach provided the opportunity to solve a radiation, damage-free structure of the apo- *Ec*-dGTPase enzyme from a limited number of crystals (Fig. 2). The XFEL structure revealed a distinctly closer contact of Mn^{2+} coordination toward the HD motif compared with an X-ray apo- structure and two previously published structures (20). Comparisons between the apo- and the dGTP-bound structures show that conformational changes in the active site of *Ec*-dGTPase allow substrate binding. Such conformational changes involve (*i*) rigid body displacements that contract and expand the substrate cage to accommodate dGTP and (*ii*) individual residue motions to establish hydrogen bonds with the substrates. Moreover, remodeling of the binding pocket upon dGTP, but not GTP, binding reveals a "moldable" active site where conformational changes are coupled to selectivity.

The structure of *Ec*-dGTPase sheds light on the mechanism of nucleotide selectivity in dNTPases. The dNTPase activity of SAMHD1 is regulated by dGTP or GTP/dNTP binding at its primary/secondary allosteric sites, respectively, and is mediated

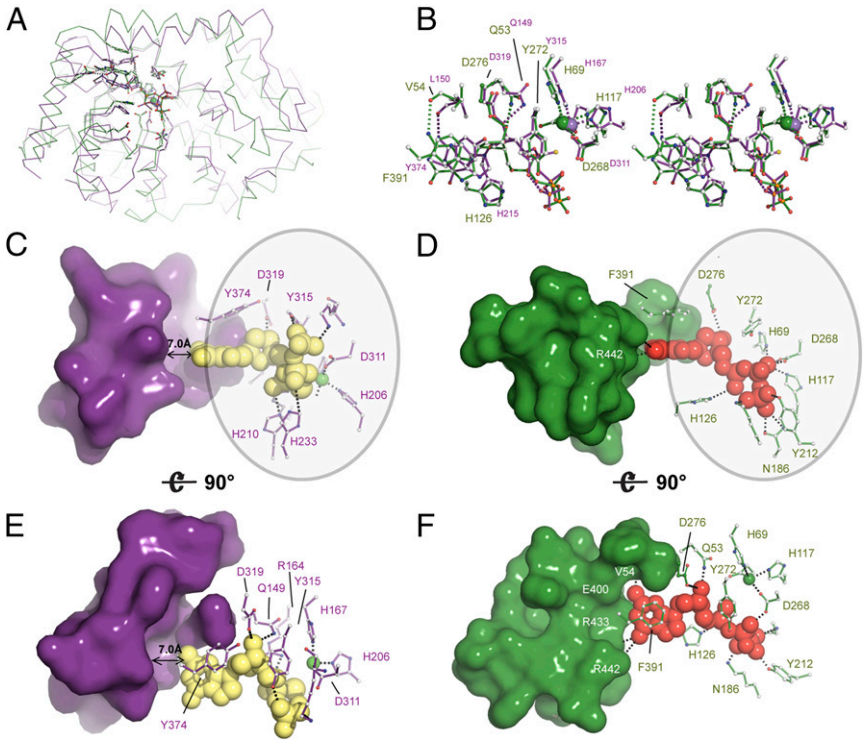

Fig. 5. Structural and enzymatic insight into the mechanism of *Ec*-dGTPase activity. (*A*) Ribbon representation of the overlay between SAMHD1 (PDB ID code 4BZC) (purple) and *Ec*-dGTPase (green) illustrating fold conservation of the enzymatic cores. (*B*) Stereo and ball-and-stick representation of the overlay between SAMHD1 and *Ec*-dGTPase active sites illustrating residue type and geometry conservation. (*C* and *E*) Surface and ball-and-stick representation of SAMHD1 active-site residues illustrating that most contacts with the dNTP involve interaction with the ribose, the phosphates, and the purine or pyrimidine ring (circle). No interactions with SAMHD1 residues that could confer specificity are possible since a 7-Å gap separates them from the dNTP. Thus, dNTPases bind shared motifs *D* and *F*. A similar set of interactions takes place in dGTPase; however, dGTP selectivity occurs through formation of four hydrogen bonds.

by tetramerization (40). The active form of SAMHD1 can bind and hydrolyze all four dNTPs with similar affinities and K_{cat} (41). Structural studies have revealed the mechanism of nucleotide binding and have shown that the shape of the catalytic pocket remains nearly identical upon binding of the four dNTP substrates (12). Overlay of the *Ec*-dGTPase and SAMHD1 structures shows that, in addition to sharing similar active-site architectures (Fig. 5*A*), HD motif residues and those involved in stacking, 3′OH discrimination, contacts with the sugar moiety, and catalysis are highly conserved (Fig. 5*B*). These interactions provide stabilization of the purine or pyrimidine rings and the ribose and phosphates, but do not allow nucleotide-type discrimination. Thus, whereas *Ec*-dGTPase residues at the nucleotide ring end of the binding pocket mimic Watson–Crick interactions with the amine or ketone groups of dGTP, SAMHD1 residues are separated by a 7-Å cleft from the dNTPs (Fig. 5 *C*–*F*). Indeed, previous high-resolution structures of nucleotide-bound SAMHD1 show that water molecules bridge interactions between the nucleotide ring and active-site residues (PDB ID code 4TNQ) (11), thus abolishing nucleotide-type discrimination.

Given that the activity of SAMHD1 is regulated by its primary/secondary allosteric sites, questions remain about the existence of an allosteric site in dGTPases. Enzymatic studies showed a threefold decrease in the apparent K_m (but had no effect on V_{max}) of *Ec*-dGTPase bound to ssDNA, reflecting substrate-binding enhancement (20). Moreover, the crystal structure revealed that ssDNA (found at the interface of two monomers ∼25 Å away from the active site) triggered conformational changes affecting the catalytically essential Tyr^{272} (*SI Appendix*, Fig. S2*C*). The structure of *Ec*-dGTPase bound to dGTP sheds light on this matter. Comparisons between the active-site residues of the apo-, dGTP-, and ssDNA-bound forms illustrate that the later combines features of the apo- and dGTP-bound structures (*SI Appendix*, Fig. S5). The net effect of ssDNA binding is an increase in the volume of the binding pocket by opening the tyrosine "gate" and hence improving binding efficiency, reconciling the observed threefold decrease in K_m.

Altogether, we utilized a combination of XFEL and chemical cross-linking methods to successfully reveal the molecular basis of *Ec*-dGTPase substrate recognition and the regulation mechanism. Together with the limited known structures of dNTPases in both prokaryotic and eukaryotic organisms, our results provide structural insight into the metabolic regulation of tightly controlled dNTP pools in DNA replication and cellular survival.

Methods

Cloning, Protein Purification, and Crystallization. The cDNA encoding wild-type *Ec*-dGTPase was a gift from Charles C. Richardson (Harvard Medical School, Boston, MA). It was cloned into the pET21 vector with a His-tag at the N terminus. Site-specific mutants of *Ec*-dGTPase were prepared using QuikChange mutagenesis kits (Agilent). Wild-type and mutant *Ec*-dGTPase proteins were expressed and purified as previously described (40). Before crystallization, *Ec*-dGTPase was buffer exchanged into a solution containing 20 mM Tris·HCl, pH 8.0, 200 mM NaCl, 0.02% azide, and 3% glycerol; 2 mM $MnCl_2$ was added to the solution after we confirmed that Mn^{2+} anomalous signal is present in the crystal. Crystals were grown at 16 °C with the sitting drop vapor diffusion method by mixture of 2 μL protein (15 mg/mL) with 2 μL crystallization buffer (100 mM Tris·HCl, pH 8.0, 1.6 M $AmSO_4$). Crystals were improved by dehydration in 3.5 M $AmSO_4$ (100 mM Tris·HCl, pH 8.0).

Crystal Growth and Mounting on MCHs. Purification, assembly, and crystallization of RNA Pol II–Spt4/5 complexes was followed as previously described (38). To mount crystals onto MCHs (Fig. 1*A*), crystals were first cryo-protected with increasing concentrations of mother liquor. Crystal drops were increased to ∼10 μL to prevent dehydration during the loading process, and MCHs were used to penetrate the drop and extract the randomly oriented crystals. For larger *Ec*-dGTPase macrocrystals (300 × 300 × 200 μm), 8 μL of cryo-solution was pipetted onto the MCH, followed by manual mounting onto the MCH via loop transfer or pipetting. To improve visualization and decrease background diffraction from solvent, excess fluid was carefully removed from MCHs using filter paper. Optimization of this step is crucial, as wicking away excess solvent may also result in the loss of crystalline sample.

Brightfield and UV-Microscopy Imaging and Crystal Identification. Brightfield and UV microscopy were employed to identify and locate crystals in relation to the MCH reference points (*SI Appendix*, Figs. S1 and S2). To this end, MCHs were placed on the stage of the JANSi UVEX UV-microscope, and after focus adjustment, brightfield and UV images covering the entire area of the MCH were acquired with the nominal 5× objective using 0.1- and 1-s exposure times, respectively. After image acquisition, the crystals and MCHs were immediately flash-cooled in a liquid nitrogen bath and transferred into a SSRL cassette. A macro to detect crystals was developed using ImageJ, a public domain, Java-based image-processing program developed by the NIH (42). ImageJ Macro details are described in *SI Appendix, Supplemental Methods*.

Postcrystallization Cross-Linking of *E. coli* dGTPase for Ligand Soaking. *Ec*-dGTPase crystals grown in 0.1 M Tris·HCl, pH 8.0, and 1.6 M ammonium sulfate were transferred step-wise into 4 M K/Na phosphate, pH 5.5, and 0.1 M Hepes, pH 8.0. After overnight incubation, glutaraldehyde was added to the reservoir at a final concentration of 2.5%, and cross-linking proceeded for 2 h before quenching with the addition of 0.1 M Tris·HCl, pH 8.0. Cross-linked crystals were washed thoroughly with low-salt reservoir (20 mM Tris·HCl, pH 8.0, 0.2 M sodium chloride, 2 mM manganese chloride, 0.02% azide, 3% glycerol) amenable to ligand soaking and incubated overnight with reservoir +30% glycerol. Ligand (dGTP or dGTP-1-thiol) with 5 mM final concentrations were added to the crystals and incubated overnight before flash-freezing in liquid nitrogen.

Automated Data Collection Using MCHs at the LCLS. Before the experiment, a reference file (*SI Appendix*, Table S1) containing crystal coordinates and coordinates of four reference points for each MCH stored in a 96-sample pin storage cassette was read into the *DCS/BLU-ICE* beam line control software (43). During the day of the experiment, the SAM robot (44) was used to mount each MCH onto the beamline goniometer followed by a manual, semiautomated alignment procedure where the MCH is rotated face on to the on-axis microscope and the four reference markers are clicked in a clockwise order from within a video display of the software interface. Following this procedure, the location of the crystal coordinates is displayed over the video image of the mount (*SI Appendix*, Fig. S1*E*) and are visually inspected. If necessary, a graphical interface enables the experimenter to remove or shift egregious crystal positions or shift the location of the reference points to improve accuracy. Updated crystal positions are stored, and the user is prompted to begin automated data collection. During automated data collection, a crystal is translated into the beam position between each X-ray pulse. This process was repeated for each MCHs in the cassette.

Diffraction experiments on *Ec*-dGTPase and Pol II complexes were done using 9.5-keV X-ray pulses with a 40-fs duration and an 8-μm beam focus at the X-ray interaction point. Diffraction images were recorded on a Rayonix MX325 detector and processed using the cctbx.xfel software package (45, 46). Synchrotron-based X-ray diffraction experiments of single dGTPase crystals were performed on SSRL beamline BL12-2 and the APS beamlines 22ID and 23IDD. Data were processed using XDS and SCALA software packages (47, 48). Single anomalous diffraction experiments of selenium–methionine-labeled dGTPase crystals were collected at 12.656 keV with inverse beam every 15° of oscillation data.

Structure Determination and Refinement. Selenium substructures were determined with SHELXC/D (49), using a resolution cutoff of 4.4 Å corresponding to a CCanom of 0.301. Substructure solutions were utilized in the CRANK pipeline (50), resulting in an initial, experimentally phased structure of *Ec*-dGTPase (*SI Appendix*, Fig. S5*A*), which was then manually built in Coot and refined in BUSTER. Subsequent *Ec*-dGTPase apo- (XFEL), GTP-bound, dGTP-1-thiol, and dGTP-bound structures were solved by PHASER (51) using the Se-Met structure as a search model. All structures were refined using Phenix (52) and BUSTER (53), followed by several cycles of manual refinement in Coot (54, 55). All superpositions and figures were rendered in PyMOL. Potential hydrogen bonds were assigned using a distance of <3.5 Å and an A-D-H angle of >90°, while the maximum distance allowed for a van der Waals interaction was 4.0 Å.

Enzymatic Assay of Ec-dGTPase Activity. Purified wild-type and active-site variants were dialyzed overnight into reaction buffer (20 mM Tris, pH 7.8, 50 mM NaCl, 3% glycerol, 5 mM $MgCl_2$) and concentrated to 2 mg/mL. For phosphohydrolase experiments, 2 μM enzyme was incubated with 100 μM dGTP (TriLink Biotech) at room temperature. Enzymatic activity was monitored at 5-, 10-, 30-, 60-, and 120-min time points by quenching the reaction

with 50 mM EDTA. Analysis of the deoxyguanosine product at the various time points was achieved by reverse-phase HPLC. Briefly, quenched reactions were injected into a C18 M column (Phenomenex) against 10 mM ammonium phosphate (pH 7.8) and 5% methanol, and the deoxyguanosine product was eluted with a gradient to 30% methanol. Individual peak heights were integrated and compared between *Ec*-dGTPase constructs. To test the effect of GTP on enzymatic activity, enzyme was assayed in a similar manner in the presence of 100 μM dGTP and increasing concentrations of GTP (0–2 mM).

To test the enzymatic activity of cross-linked crystals, we washed glutaraldehyde cross-linked crystals extensively with low-salt reservoir buffer (20 mM Tris-HCl pH 8.0, 0.2 M sodium chloride, 2 mM manganese chloride, 0.02% azide, 3% glycerol) as described above. Enzymatic activity was monitored by incubating washed crystals in the presence of 100 μM dGTP for 60 min at 37 °C. Reverse-phase HPLC was used to analyze the deoxyguanosine product for cross-linked enzyme in crystals, unmodified enzyme in solution, and unmodified enzyme in solution in the presence of 500 μM GTP.

ACKNOWLEDGMENTS. We thank Michael Becker and Craig Ogata (GM/CA at Argonne National Laboratory); Irimpan Mathews, Clyde Smith, and Ana Gonzalez at the Stanford Synchrotron Radiation Lightsource (SSRL), for their support during data collection; D. Lee for home-source X-ray technical support; and Charles C. Richardson (Harvard University) for providing cDNA of dGTPase. This work was supported by NIH Grants R01GM116642 (to J.A.), R01GM112686 and P50GM082251 (to G.C.), and R01GM117126 (to N.K.S.). G.C. also acknowledges support from BioXFEL-STC1231306. Use of the LCLS and SSRL SLAC National Accelerator Laboratory is supported by the US Department of Energy, Office of Science, Office of Basic Energy Sciences under Contract DE-AC02-76SF00515. The SSRL Structural Molecular Biology Program is supported by the Department of Energy, Office of Biological and Environmental Research and by the NIH, National Institute of General Medical Sciences (NIGMS) (including Grant P41GM103393). The contents of this publication are solely the responsibility of the authors and do not necessarily represent the official views of the NIGMS or NIH.

1. Meuth M (1984) The genetic consequences of nucleotide precursor pool imbalance in mammalian cells. *Mutat Res* 126:107–112.
2. Seto D, Bhatnagar SK, Bessman MJ (1988) The purification and properties of deoxyguanosine triphosphate triphosphohydrolase from Escherichia coli. *J Biol Chem* 263: 1494–1499.
3. Nordlund P, Reichard P (2006) Ribonucleotide reductases. *Annu Rev Biochem* 75: 681–706.
4. Kunz BA, et al. (1994) International commission for protection against environmental mutagens and carcinogens. Deoxyribonucleoside triphosphate levels: A critical factor in the maintenance of genetic stability. *Mutat Res* 318:1–64.
5. Wheeler LJ, Rajagopal I, Mathews CK (2005) Stimulation of mutagenesis by proportional deoxyribonucleoside triphosphate accumulation in Escherichia coli. *DNA Repair (Amst)* 4:1450–1456.
6. Gon S, et al. (2006) A novel regulatory mechanism couples deoxyribonucleotide synthesis and DNA replication in Escherichia coli. *EMBO J* 25:1137–1147.
7. Kornberg SR, Lehman IR, Bessman MJ, Simms ES, Kornberg A (1958) Enzymatic cleavage of deoxyguanosine triphosphate to deoxyguanosine and tripolyphosphate. *J Biol Chem* 233:159–162.
8. Huber HE, Beauchamp BB, Richardson CC (1988) Escherichia coli dGTP triphosphohydrolase is inhibited by gene 1.2 protein of bacteriophage T7. *J Biol Chem* 263: 13549–13556.
9. Kondo N, Kuramitsu S, Masui R (2004) Biochemical characterization of TT1383 from Thermus thermophilus identifies a novel dNTP triphosphohydrolase activity stimulated by dATP and dTTP. *J Biochem* 136:221–231.
10. Vorontsov II, et al. (2014) Mechanisms of allosteric activation and inhibition of the deoxyribonucleoside triphosphate triphosphohydrolase from Enterococcus faecalis. *J Biol Chem* 289:2815–2824.
11. Ji X, Tang C, Zhao Q, Wang W, Xiong Y (2014) Structural basis of cellular dNTP regulation by SAMHD1. *Proc Natl Acad Sci USA* 111:E4305–E4314.
12. Koharudin LMI, et al. (2014) Structural basis of allosteric activation of sterile α motif and histidine-aspartate domain-containing protein 1 (SAMHD1) by nucleoside triphosphates. *J Biol Chem* 289:32617–32627.
13. Aravind L, Koonin EV (1998) The HD domain defines a new superfamily of metal-dependent phosphohydrolases. *Trends Biochem Sci* 23:469–472.
14. Laguette N, et al. (2011) SAMHD1 is the dendritic- and myeloid-cell-specific HIV-1 restriction factor counteracted by Vpx. *Nature* 474:654–657.
15. Kondo N, et al. (2007) Structure of dNTP-inducible dNTP triphosphohydrolase: Insight into broad specificity for dNTPs and triphosphohydrolase-type hydrolysis. *Acta Crystallogr D Biol Crystallogr* 63:230–239.
16. Nakai H, Richardson CC (1990) The gene 1.2 protein of bacteriophage T7 interacts with the Escherichia coli dGTP triphosphohydrolase to form a GTP-binding protein. *J Biol Chem* 265:4411–4419.
17. Zhu C, et al. (2013) Structural insight into dGTP-dependent activation of tetrameric SAMHD1 deoxynucleoside triphosphate triphosphohydrolase. *Nat Commun* 4:2722.
18. Titz B, Häuser R, Engelbrecher A, Uetz P (2007) The Escherichia coli protein YjjG is a house-cleaning nucleotidase in vivo. *FEMS Microbiol Lett* 270:49–57.
19. Mega R, Kondo N, Nakagawa N, Kuramitsu S, Masui R (2009) Two dNTP triphosphohydrolases from Pseudomonas aeruginosa possess diverse substrate specificities. *FEBS J* 276:3211–3221.
20. Carter M, et al. (2015) Crystal structure, biochemical and cellular activities demonstrate separate functions of MTH1 and MTH2. *Nat Commun* 6:7871.
21. Singh D, et al. (2015) Structure of Escherichia coli dGTP triphosphohydrolase: A hexameric enzyme with DNA effector molecules. *J Biol Chem* 290:10418–10429.
22. Wurgler SM, Richardson CC (1993) DNA binding properties of the deoxyguanosine triphosphate triphosphohydrolase of Escherichia coli. *J Biol Chem* 268:20046–20054.
23. Cohen AE, et al. (2014) Goniometer-based femtosecond crystallography with X-ray free electron lasers. *Proc Natl Acad Sci USA* 111:17122–17127.
24. Hirata K, et al. (2014) Determination of damage-free crystal structure of an X-ray-sensitive protein using an XFEL. *Nat Methods* 11:734–736.
25. Schlichting I, Miao J (2012) Emerging opportunities in structural biology with X-ray free-electron lasers. *Curr Opin Struct Biol* 22:613–626.
26. Baxter EL, et al. (2016) High-density grids for efficient data collection from multiple crystals. *Acta Crystallogr D Struct Biol* 72:2–11.
27. Lyubimov AY, et al. (2015) Capture and X-ray diffraction studies of protein microcrystals in a microfluidic trap array. *Acta Crystallogr D Biol Crystallogr* 71:928–940.
28. Hunter MS, et al. (2014) Fixed-target protein serial microcrystallography with an X-ray free electron laser. *Sci Rep* 4:6026.
29. Mueller C, et al. (2015) Fixed target matrix for femtosecond time-resolved and in situ serial micro-crystallography. *Struct Dyn* 2:054302.
30. Murray TD, et al. (2015) A high-transparency, micro-patternable chip for X-ray diffraction analysis of microcrystals under native growth conditions. *Acta Crystallogr D Biol Crystallogr* 71:1987–1997.
31. Roedig P, et al. (2015) A micro-patterned silicon chip as sample holder for macromolecular crystallography experiments with minimal background scattering. *Sci Rep* 5:10451.
32. Barnes CO, et al. (2018) Structural characterization of a highly-potent V3-glycan broadly neutralizing antibody bound to natively-glycosylated HIV-1 envelope. *Nat Commun* 9:1251.
33. Stevenson HP, et al. (2016) Transmission electron microscopy for the evaluation and optimization of crystal growth. *Acta Crystallogr D Struct Biol* 72:603–615.
34. Zhou Q, et al. (2015) Architecture of the synaptotagmin-SNARE machinery for neuronal exocytosis. *Nature* 525:62–67.
35. Brewster AS, et al. (2015) Indexing amyloid peptide diffraction from serial femtosecond crystallography: New algorithms for sparse patterns. *Acta Crystallogr D Biol Crystallogr* 71:357–366.
36. Gerstel M, Deane CM, Garman EF (2015) Identifying and quantifying radiation damage at the atomic level. *J Synchrotron Radiat* 22:201–212.
37. Vorontsov II, et al. (2011) Characterization of the deoxynucleotide triphosphate triphosphohydrolase (dNTPase) activity of the EF1143 protein from Enterococcus faecalis and crystal structure of the activator-substrate complex. *J Biol Chem* 286: 33158–33166.
38. Boutet S, Cohen A, Wakatsuki S (2016) The new macromolecular femtosecond crystallography (MFX) instrument at LCLS. *Synchrotron Radiat News* 29:23–28.
39. Martiel I, Muller-Werkmeister HM, Cohen AE (2019) Strategies for sample delivery for femtosecond crystallography. *Acta Crystallogr Sect D Struct Biol* 75:Sup-1–Sup-11.
40. Yan J, et al. (2013) Tetramerization of SAMHD1 is required for biological activity and inhibition of HIV infection. *J Biol Chem* 288:10406–10417.
41. Jang S, Zhou X, Ahn J (2016) Substrate specificity of SAMHD1 triphosphohydrolase activity is controlled by deoxyribonucleoside triphosphates and phosphorylation at Thr592. *Biochemistry* 55:5635–5646.
42. Girish V, Vijayalakshmi A (2004) Affordable image analysis using NIH Image/ImageJ. *Indian J Cancer* 41:47.
43. McPhillips TM, et al. (2002) Blu-ice and the distributed control system: Software for data acquisition and instrument control at macromolecular crystallography beamlines. *J Synchrotron Radiat* 9:401–406.
44. Smith CA, Cohen AE (2008) The Stanford automated mounter: Enabling high-throughput protein crystal screening at SSRL. *JALA Charlottesv Va* 13:335–343.
45. Hattne J, et al. (2014) Accurate macromolecular structures using minimal measurements from X-ray free-electron lasers. *Nat Methods* 11:545–548.
46. Lyubimov AY, et al. (2016) Advances in X-ray free electron laser (XFEL) diffraction data processing applied to the crystal structure of the synaptotagmin-1/SNARE complex. *eLife* 5:e18740.
47. Evans P (2006) Scaling and assessment of data quality. *Acta Crystallogr D Biol Crystallogr* 62:72–82.
48. Kabsch W (2010) Xds. *Acta Crystallogr D Biol Crystallogr* 66:125–132.
49. Schneider TR, Sheldrick GM (2002) Substructure solution with SHELXD. *Acta Crystallogr D Biol Crystallogr* 58:1772–1779.
50. Ness SR, de Graaff RA, Abrahams JP, Pannu NS (2004) CRANK: New methods for automated macromolecular crystal structure solution. *Structure* 12:1753–1761.
51. McCoy AJ, et al. (2007) Phaser crystallographic software. *J Appl Cryst* 40:658–674.
52. Adams PD, et al. (2010) PHENIX: A comprehensive python-based system for macromolecular structure solution. *Acta Crystallogr D Biol Crystallogr* 66:213–221.
53. Blanc E, et al. (2004) Refinement of severely incomplete structures with maximum likelihood in BUSTER-TNT. *Acta Crystallogr D Biol Crystallogr* 60:2210–2221.
54. Emsley P, Lohkamp B, Scott WG, Cowtan K (2010) Features and development of Coot. *Acta Crystallogr D Biol Crystallogr* 66:486–501.
55. Karplus PA, Diederichs K (2012) Linking crystallographic model and data quality. *Science* 336:1030–1033.